Supporting Information

Cu^{2+}-regulated reversible coordination interaction of GQDs@Tb/GMP ICP nanoparticles: Towards direct monitoring cerebrospinal acetylcholinesterase as a biomarker for cholinic brain dysfunction

Chang Liu,[a, b] Chunyu Huang,[a, b] Ruixue Ma,[a, b] Wanying Zhai,[c] Jingjing Deng,*[a, b] and Tianshu Zhou[a, b]

[a]*School of Ecological and Environmental Sciences, Shanghai Key Lab for Urban Ecological Process and Eco-Restoration, East China Normal University, 500 Dongchuan Road, Shanghai 200241, China.*

[b]*Institute of Eco-Chongming, 3663 Zhongshan Road, Shanghai 200062, China.*

[c]*Center for Yangtze Valley Water Ecology Environment Monitoring and science research of Yangtze River Administration Bureau of Ministry of Ecology and Environment, 13 Yongqing Road, Wuhan 430019, China.*

* Corresponding Authors: E-mail: jjdeng@des.ecnu.edu.cn

Tel: +86-21-54341113

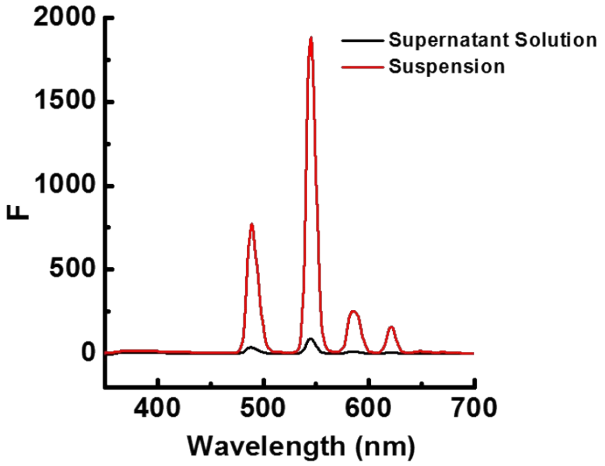

Fig. S1. Fluorescent spectra of the dispersion (1 mL) containing GQDs@Tb/GMP ICP nanoparticles (1.85 mg) after several times of washing. The curves show the fluorescent spectra of the supernatant of the dispersion (1 mL, black curve) and the GQDs@Tb/GMP ICP nanoparticles re-dispersed in water (1 mL, red curve). E_x = 300 nm.

The supernatant solution of GQDs@Tb/GMP ICP nanoparticles showed almost no fluorescent signal, indicating the free GQDs or GQDs absorbed on the surface of Tb/GMP ICP network was clearly removed.

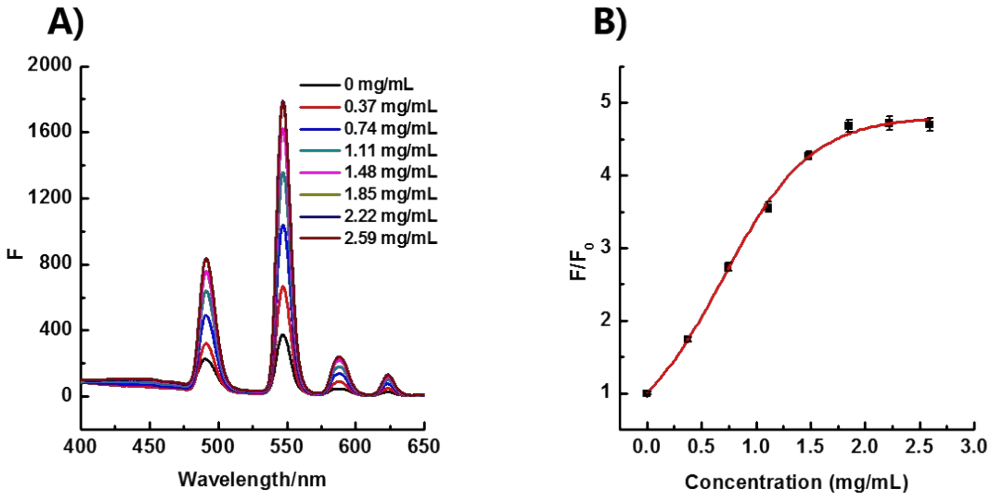

Fig. S2. (A) Fluorescent spectra of GQDs@Tb/GMP ICP nanoparticles with different concentration of GQDs (from 0 mg/mL to 2.59 mg/mL); (B) The ratio of F/F_0 versus the concentration of GQDs.

To realize the sensitive detection of AChE and OPs, the amount of the guest GQDs were optimized by adding the aqueous solution of $Tb(NO_3)_3 \cdot 6H_2O$ (2.0 mL, 10 mM) with a HEPES buffer (2.0 mL, 0.1 M, pH 7.4) containing GMP (10 mM) and different amount of GQDs (0.37, 0.74, 1.11, 1.48, 1.85, 2.22, 2.59 mg/mL). The fluorescent property of as-formed GQDs@Tb/GMP ICP nanoparticles was measured and the results were shown in Fig. S2. When the concentration was higher than 1.85 mg/mL, the fluorescence intensity of Tb^{3+} at 545 nm (F_{545}) showed no significant enhancement. Consequently, 1.85 mg/mL GQDs was chosen as the optimal guest to sensitize the fluorescence of Tb/GMP ICP nanoparticles for the further application.

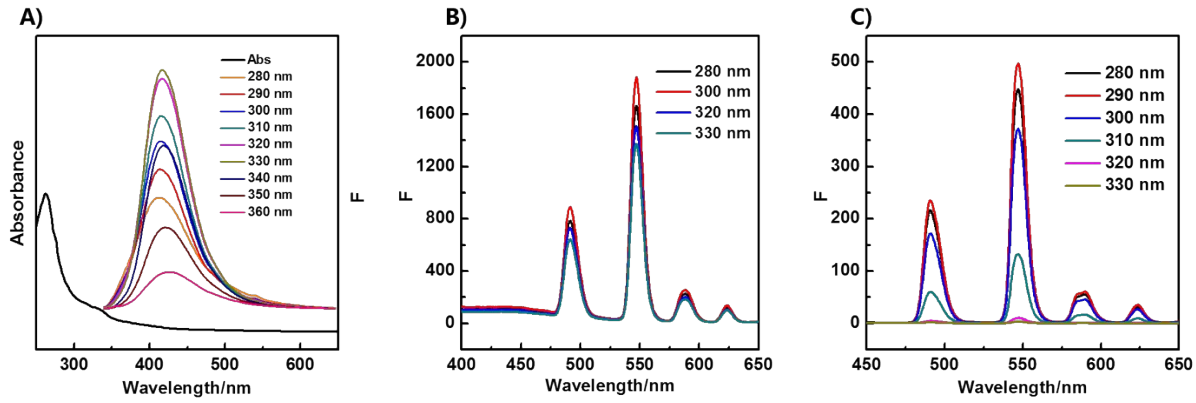

Fig. S3. (A) UV-vis absorption spectra of GQDs (left) and fluorescence emission spectra of GQDs under different excitation wavelength form 280 nm to 360 nm (right); (B) Fluorescence emission spectra of Tb/GMP ICP nanoparticles under different excitation wavelength from 280 nm to 330 nm. (C) Fluorescence emission spectra of GQDs@Tb/GMP ICP nanoparticles under different excitation wavelength from 280 nm to 330 nm.

Firstly, the UV-vis spectra of GQDs were firstly investigated. As shown in Fig. S3A, two absorption bands appeared at 240 nm and 330 nm, which may attribute to the π-π* transition of the aromatic ring structure and n-π* transition of C=O, respectively. Moreover, when the excitation wavelength increased from 280 nm to 330 nm, the emission of GQDs at 425 nm increased gradually, while the further increase of the excitation wavelength from 340 nm to 360 nm resulted in the dramatic decrease of the fluorescent intensity of GQDs. Considering the excitation wavelength for guest functionalized Tb/GMP ICPs was reported within the range 280-330 nm,[1,2] the optimal excitation wavelength for GQDs@Tb/GMP ICP nanoparticles was investigated and the results were displayed in Fig. S3B. When the excitation wavelength was set as 300 nm, the emission of sensitized GQDs@Tb/GMP ICP nanoparticles reached maximum, which was a little different with Tb/GMP ICP host (290

nm) (Fig. S3C). This may be due to the increased fluorescence emission of GQDs, which facilitated the sensitization of Tb/GMP ICPs at 300 nm. Therefore, 300 nm was selected as the optimal excitation wavelength for the following experiments in this study.

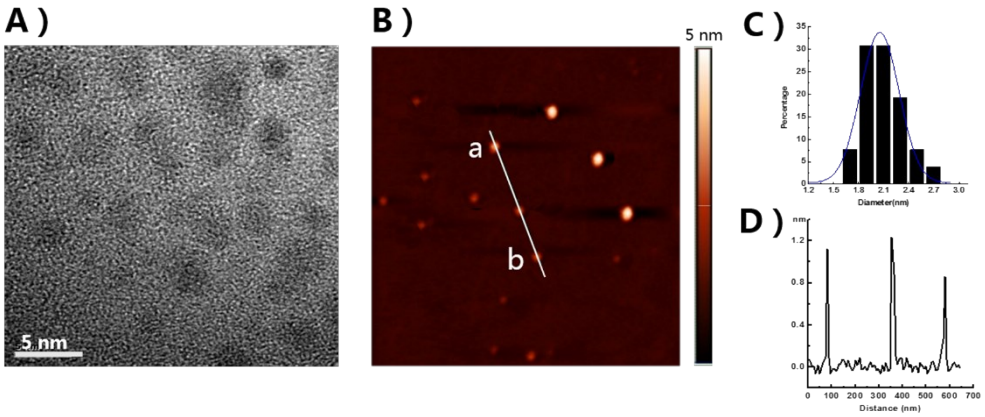

Fig. S4. (A) TEM image of GQDs; (B) AFM image of GQDs; (C) Size distribution of GQDs; (D) The height profile along the line ab indicated in (B).

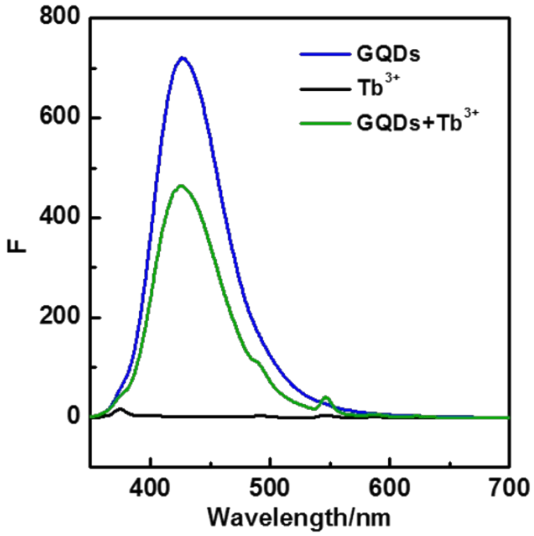

Fig. S5. Fluorescence emission spectra of GQDs (1.85 mg/mL) (blue curve), Tb^{3+} (1 mM) (black curve) and GQDs (1.85 mg/mL) + Tb^{3+} (1 mM) (green curve).

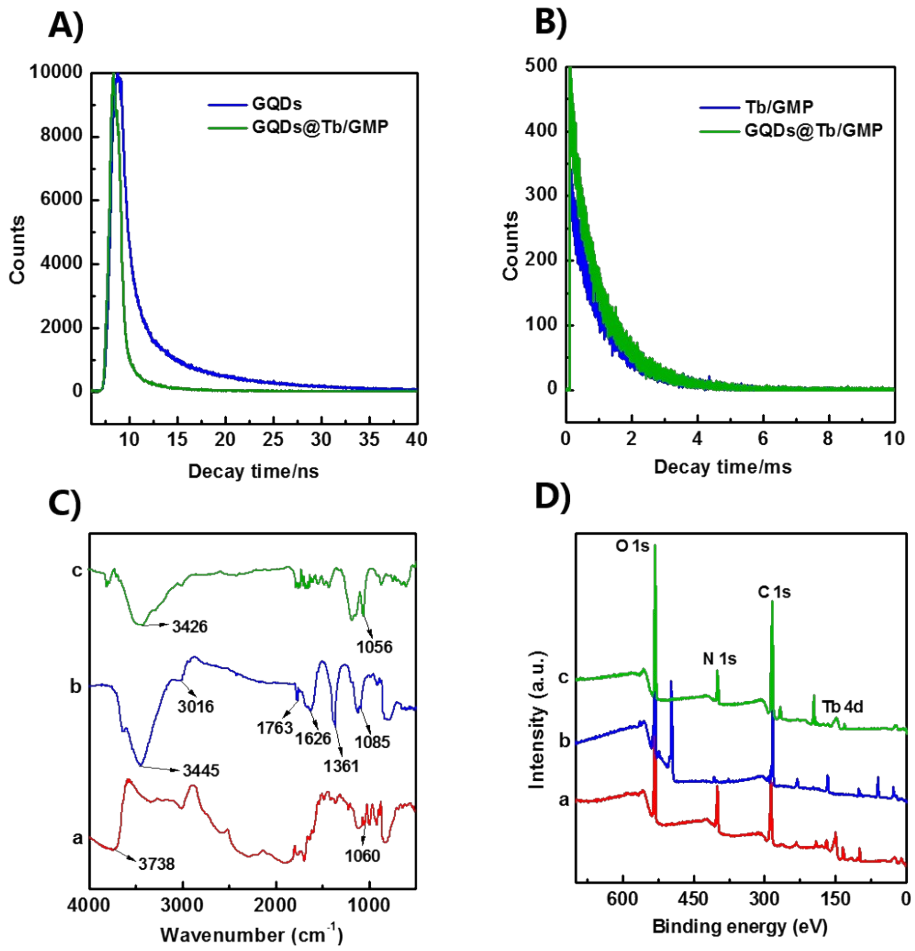

Fig. S6. (A) Fluorescence decay profiles of free CDs and GQDs@Tb/GMP ICP nanoparticles at 425 nm; (B) Fluorescence decay profiles of Tb/GMP ICP nanoparticles and GQDs@Tb/GMP ICP nanoparticles at 545 nm; FT-IR spectra (C) and XPS spectra (D) of Tb/GMP ICP nanoparticles (a, red curve), GQDs (b, blue curve) and GQDs@Tb/GMP ICP nanoparticles (c, green curve).

The fluorescence lifetimes of GQDs@Tb/GMP ICP nanoparticles at 425 nm and 545 nm were measured. As shown in Fig. S6A and B, the fluorescence lifetime of GQDs shortened from 1.98 ns to 0.98 ns after incorporation, moreover, compared with Tb/GMP ICP nanoparticles, the fluorescence lifetime of GQDs@Tb/GMP ICP nanoparticles increased from 0.82 ms to 0.98 ms, which validated the existence of electron or energy transfer from

GQDs to Tb/GMP ICP.[3,4] In addition, FTIR was also investigated to verify the interaction between GQDs and Tb/GMP ICP. As shown in Fig. S6C, For Tb/GMP ICP nanoparticles (a, red curve), the absorption peak at 3738 cm^{-1} was ascribed to the O-H stretching vibration of coordinated water molecules in the network structure of Tb/GMP.[5] Meanwhile, the characteristic peak of PO_4^{3-} of GMP appeared at 1060 cm^{-1}.[6] For free GQDs (b, blue curve), the presence of 3445 cm^{-1} and 1361 cm^{-1} confirmed the stretching and bending vibration of O-H bond. In the meantime, the absorption peaks at 1085 cm^{-1}, 1626 cm^{-1}, and 3016 cm^{-1} were also observed, which were attributed to the stretching vibration of the C-O, C=C and C-H, respectively.[7] Besides, the absorption peak at 1763 cm^{-1} were assigned to the C=O stretching vibration of carboxylic group.[8] However, upon the addition of GQDs into Tb/GMP ICP nanoparticles (Fig. S6C, c, green curve), the absence of O-H band of coordinated water molecules in the Tb/GMP ICP network structure and the slight red shift of the stretching band in GMP (1056 cm^{-1}) could be observed, accompanied by the O-H band of GQDs red-shifted to 3426 cm^{-1}, suggesting that the coordination interaction between GQDs and Tb^{3+}. Through which, the coordinated water molecules in the network structure were replaced, and the improved hydrophobic interior of the Tb/GMP ICP resulted in an efficient energy transfer from GQDs to Tb^{3+}. In addition, the π-π network nature of graphene facilitated GQDs to interact with GMP through hydrogen bonding or π-π stacking, which may also benefit for the sensitization of Tb/GMP.[9] Following, XPS measurement of the binding site of before/after encapsulation of GQDs into the Tb/GMP ICP nanoparticles were carefully analyzed. As shown in Fig. S6D, the O 1s of GQDs@Tb/GMP ICP nanoparticles exhibited a higher binding energy (532.52 eV) than

GQDs (531.7 eV), while the Tb 4d peak appeared at 150.1 eV were lower than the Tb/GMP (150.63 eV), which confirmed the formation of Tb-O coordination bonds between the carboxyl group of GQDs and Tb^{3+}.[10] Meanwhile, the binding energy of N 1s (401.19 eV) in GQDs@Tb/GMP was higher than that of Tb/GMP (399.82 eV), indicating the non-covalent interaction between GQDs and GMP may also promote the electron transfer from N7 moieties of the base in GMP to Tb^{3+}, which eventually resulted in the unique enhancement of the green luminescence of Tb^{3+} and the diminished blue fluorescence of GQDs under host confinement induced aggregation-caused quenching effect simultaneously.

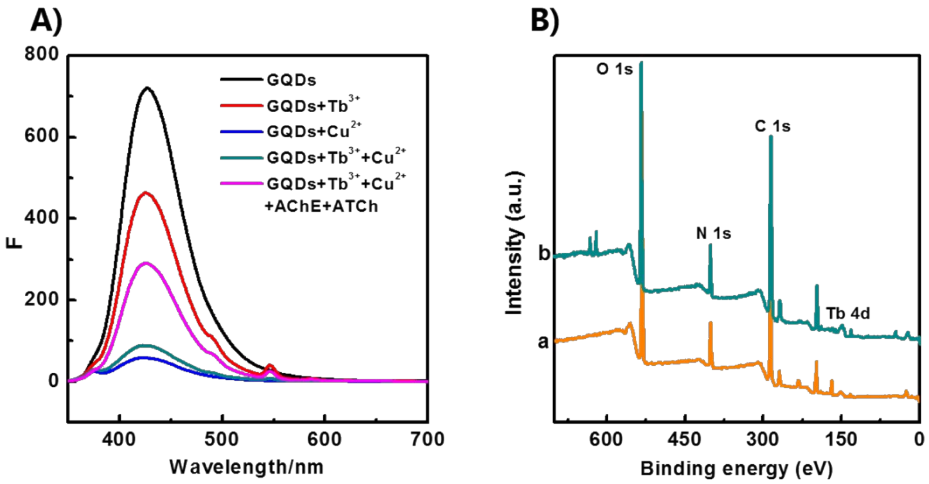

Fig. S7. (A) Fluorescence emission spectra of GQDs (1.85 mg/mL) (black curve), GQDs (1.85 mg/mL) + Tb^{3+} (1 mM) (red curve), GQDs (1.85 mg/mL) + Cu^{2+} (1 mM) (blue curve), GQDs (1.85 mg/mL) + Tb^{3+} (1 mM) + Cu^{2+} (1 mM) (bluish-green curve) and GQDs (1.85 mg/mL) + Tb^{3+} (1 mM) + Cu^{2+} (1 mM) + AChE (400 mU/mL) + ATCh (1 mM) (purplish-red, curve); (B) XPS spectra of GQDs@Tb/GMP + Cu^{2+} (a, orange curve) and GQDs@Tb/GMP + Cu^{2+} + AChE + ATCh (b, bluish-green curve).

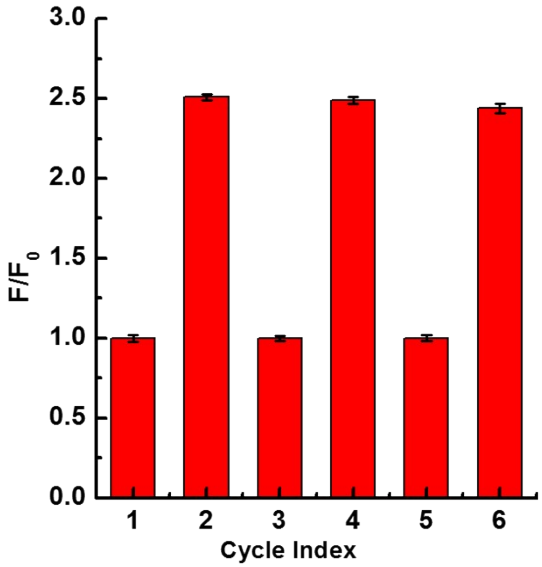

Fig. S8. Reversible F/F_0 changes of GQDs@Tb/GMP ICP nanoparticles upon cyclic treatment with Cu^{2+} and AChE-treated ATCh.

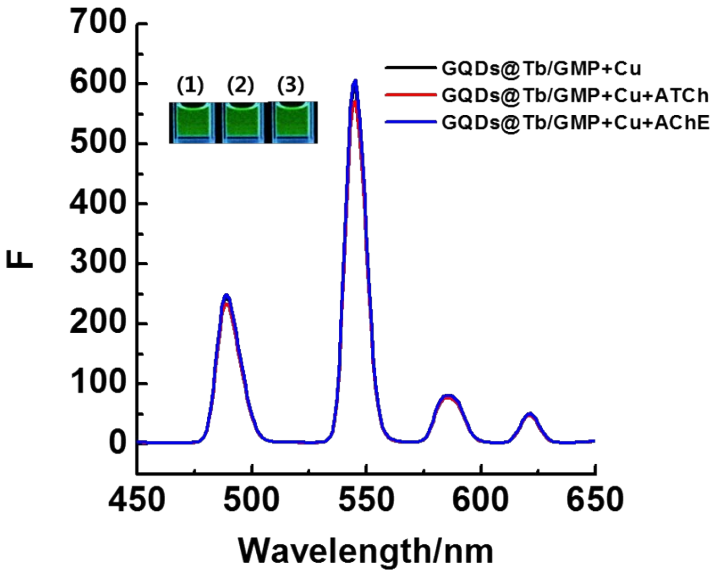

Fig. S9. Fluorescence emission spectra of GQDs@Tb/GMP+Cu^{2+} (black curve), GQDs@Tb/GMP+Cu^{2+}+ATCh (red curve) and GQDs@Tb/GMP+Cu^{2+}+AChE (blue curve). Inset: photographs of GQDs@Tb/GMP+Cu^{2+} (1), GQDs@Tb/GMP+Cu^{2+}+ATCh (2) and GQDs@Tb/GMP+Cu^{2+}+AChE (3).

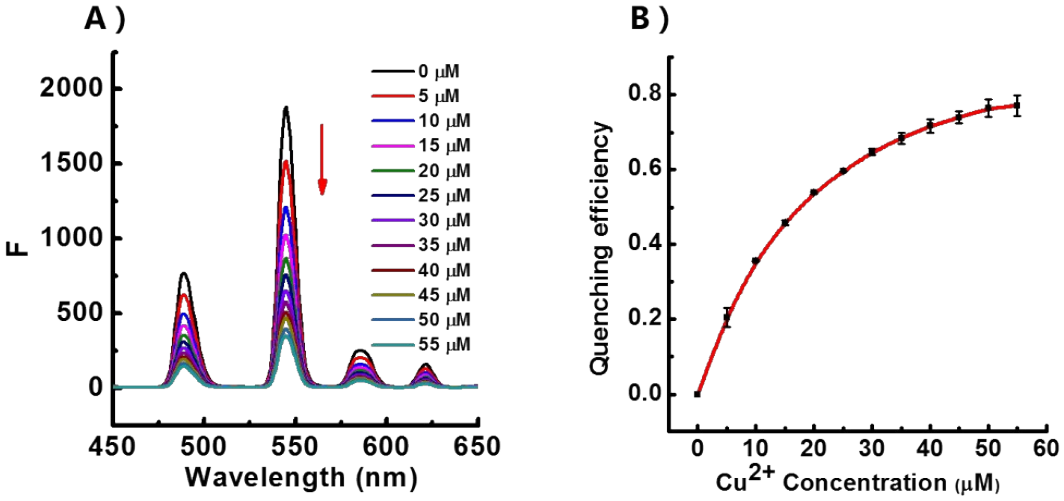

Fig. S10. (A) Fluorescence emission spectra of GQDs@Tb/GMP ICP nanoparticles (1.85 mg/mL) in the presence of Cu^{2+} with different concentration; (B) Fluorescence quenching efficiency versus the concentration of Cu^{2+}.

Since the method was established on enzymatic reaction regulated coordination interaction, the suitable concentration of the competitive Cu^{2+} will ensure optimal performance of the GQDs@Tb/GMP ICP nanoparticles for AChE detection. As shown in Fig. S10A, B, the fluorescence intensity of GQDs@Tb/GMP ICP nanoparticles decreases with increasing concentration of Cu^{2+}. When the concentration of Cu^{2+} was higher than 30 μM, the fluorescence of GQDs@Tb/GMP ICP nanoparticles decreased less sensitively as compared with the case when a lower concentration of Cu^{2+} was used. As a result, we optimized the concentration of Cu^{2+} at 30 μM to realize AChE determination with high sensitivity and low background.

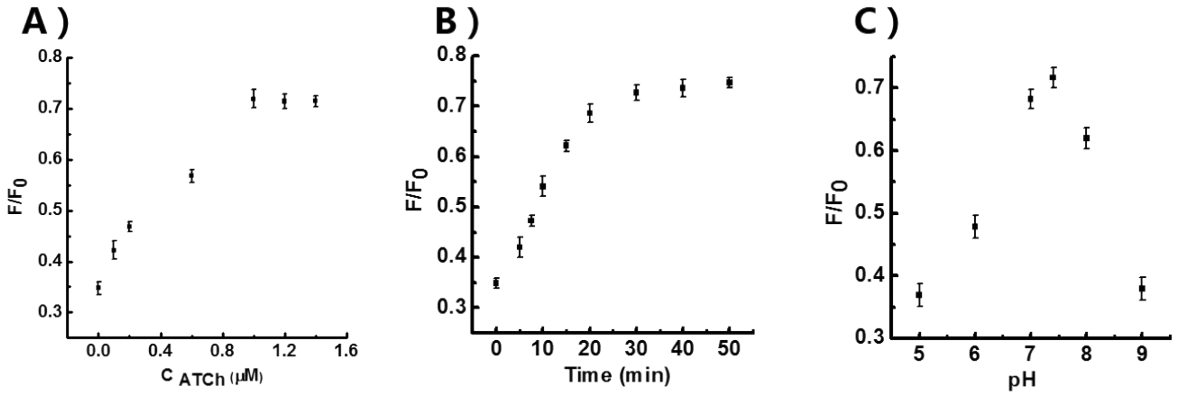

Fig. S11. Effects of the concentration of ATCh (A), the reaction time between AChE and ATCh (B) and pH (C).

Fig. S11A showed the variation of the fluorescence of GQDs@Tb/GMP ICP nanoparticles with the presence of AChE (200 mU/mL) treated ATCh with different concentrations. As could be seen, when the concentration of ATCh was higher than 1 mM, the fluorescence recovery of GQDs@Tb/GMP ICPs reached maximum and remained almost unchanged, while high concentration of ATCh may result in a negative impact on the detection of sensitive enzyme activity, the concentration of ATCh was rationally optimized at 1 mM. The influence of the incubation time was next investigated. As displayed in Fig. S11B, the fluorescence intensity gradually increased with prolonging incubation time and reached maximum at 35 min, which meant the enzymatic reaction has almost been completed. Hence, we choose 35 min as reaction time for adequate enzymatic reaction. Moreover, as shown in Fig. S11C, when thus, pH value was chosen as the physiological pH (pH=7.4), the fluorescence response of GQDs@Tb/GMP ICPs for AChE was biggest. Also taken cerebrospinal AChE detection for the consideration, 7.4 was settled as optimal pH for enzymatic reaction.

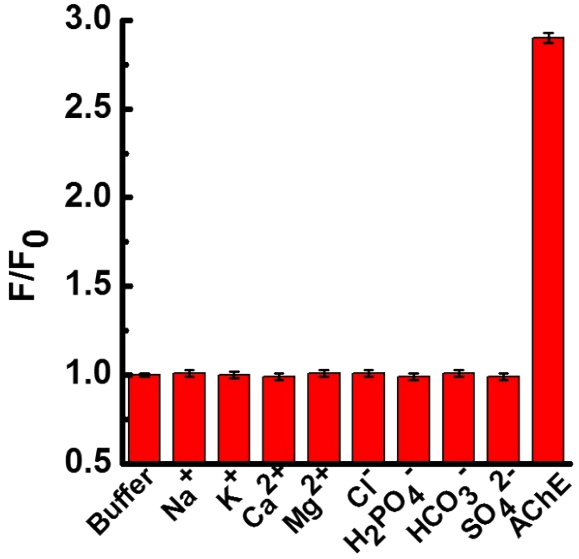

Fig. S12. The ratio of F/F_0 versus different cations and anions in aCSF. From left to right: Buffer, Na^+ (126 mM), K^+ (2.4 mM), Ca^{2+} (1.1 mM), Mg^{2+} (0.85 mM), Cl^- (126 mM), $H_2PO_4^-$ (0.5 mM), HCO_3^- (27.5 mM), SO_4^{2-} (0.5 mM) and AChE (400 mU/mL). Error bars indicate standard deviations (n = 3).

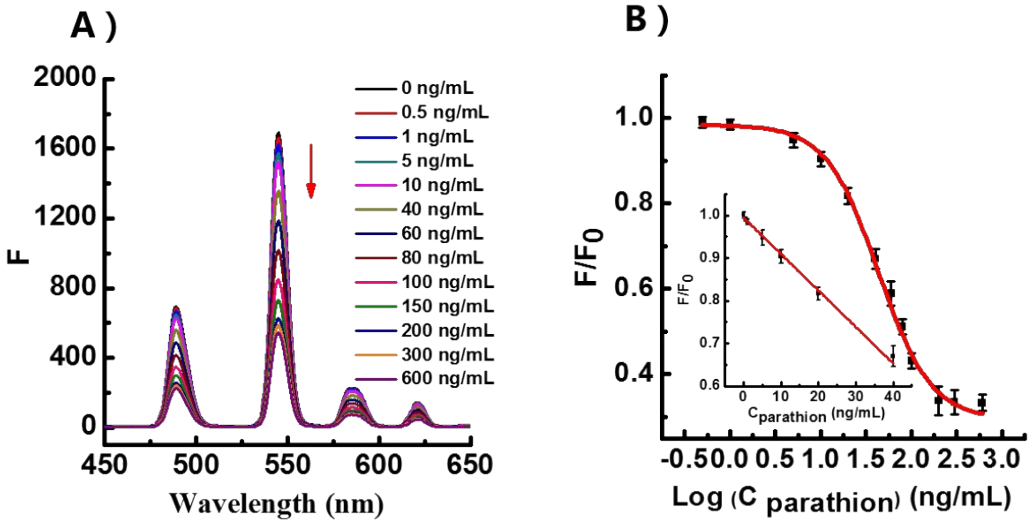

Fig. S13. (A) Fluorescent spectra of the dispersion of GQDs@Tb/GMP ICP nanoparticles containing Cu^{2+} with the addition of ATCh catalyzed by different concentration of parathion-treated AChE (400 mU/mL); (B) Kinetic plot of F/F_0 value versus the logarithm of parathion concentration. Inset: F/F_0 value versus parathion concentration. Error bars indicate standard deviations (n = 3).

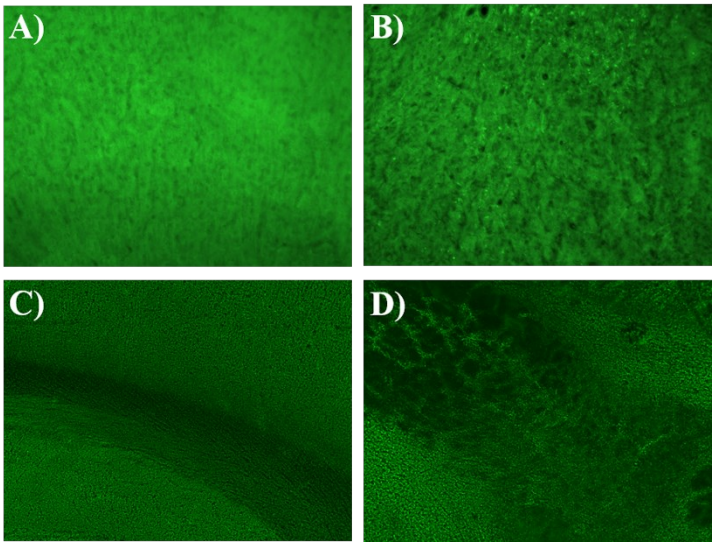

Fig. S14. Images of prefrontal cortex stained with thioflavin S. Normal group (A), AD group (B); Images of hippocampal vertebral cells stained with immunofluorescent antibody. Normal group (C), AD group (D).

As pointed out previously, the formation of amyloid plaques in brain tissues were the crucial evidence of AD pathology. The images of brain pathological sections obtained by frozen section method were displayed in Fig. S14. As shown in Fig. S14A, no apparent amyloid plaques were observed in the prefrontal cortex of normal rats, while large numbers of amyloid plaques were observed in the prefrontal cortex of AD model rats (Fig. S14B). Furthermore, Fig. S14C also showed that the hippocampal vertebral cells in the brain of normal rats were arranged regularly and tightly. However, the hippocampal vertebral cells of AD model rats were irregularly arranged and the gap between cells was larger (Fig. S14D). The above results confirmed the successful modeling of AD rats.

Table S1. A comparison of fluorescent methods for the detection of AChE.

Methods	Sensor	Enzyme	Detection limit (mU/mL)	Real samples	Refs.
Fluorescence	Supramolecular probe	AChE	5	None	11
Fluorescence	Polyethyleneimine -protected copper nanoclusters	AChE	1.38	None	12
Fluorescence	Carbon dots	AChE	0.1	None	13
Fluorescence	BSA-AuAgNCs	AChE	0.15	None	14
Fluorescence	Polydiacetylene supramolecules	AChE	1	None	15
Fluorescence	GSH-AuNCs	AChE	0.03	None	16
Fluorescence	Phenoxy-modified dextran	AChE	0.27	None	17
Fluorescence	GQDs@Tb/GMP	AChE	0.033	Cerebrospinal fluid	This work

References

(1) P. C. Huang, F. Y. Wu and L. Q. Mao, *Anal. Chem.* 2015, **87**, 6834-6841.

(2) J. J. Deng, P. Wu, Y. X. Wang and L. Q. Mao, *Anal. Chem.* 2015, **87**, 3080-3086.

(3) A. Cao, Z. Liu, S. S. Chu, M. H. Wu, Z. M. Ye, Z. W. Cai, Y. L. Chang, S. F. Wang, Q. H. Gong and Y. F. Liu, *Adv. Mater.*, 2010, **22**, 103-106.

(4) F. Y. Wang, X. Hu, J. Hu, Q. Q, Peng, B. Z. Zheng, J. Du and D. Xiao, *J. Mater. Chem. B,* 2018, **6**, 6008-6015.

(5) C. Liu, D. K. Lu, X. R. You, G. Y. Shi, J. J. Deng and T. S. Zhou, *Anal. Chim. Acta*, 2020, **1105**, 147-154.

(6) J. Ou-Yang, C. Y. Li, Y. F. Li, B. Yang and S. J. Li, *Sensor Actuat B: Chem.*, 2018, **255**, 3355-3363.

(7) Y. H. Song, H. Y. Liu, H. L. Tan, F. G. Xu, J. B. Jia, L. X. Zhang, Z. Li and L. Wang, *Anal. Chem.*, 2014, **86**, 1980-1987.

(8) X. C. Zhao, F. Hao, D. W. Lu, W. Liu, Q. F. Zhou and G. B. Jiang, *ACS Appl. Mater. Inter.*, 2015, **7**, 18880-18890.

(9) Y. J. Tong, L. D. Yu, L. L. Wu, S. P. Cao, Y. L. Guo, R. P. Liang and J. D. Qiu, *ACS Sustainable Chem. Eng.*, 2018, **6**, 9333-9341.

(10) S. Qin and B. Yan, *Sens. Actuators B: Chem.,* 2018, **272**, 510-517.

(11) C. H. He, H. P. Zhou, E. Hussain, Y. Y. Zhang, N. Niu, Y. H. Li, Y. Q. Ma and C. Yu, *RSC Adv.*, 2018, **8**, 12785-12790.

(12) J. L. Yang, N. Z. Song, X. J. Lv and Q. Jia, *Sensor. Actuat. B: Chem.*, 2018, **259**, 226-232.

(13) X. M. Xu, Y. Cen, G. H. Xu, F. D. Wei, M. L. Shi and Q. Hu, *Biosens. Bioelectron.*, 2019, **131**, 232-236.

(14) R. Liu, Z. Y. Wu, Y. L. Yang, S. Z. Liao and R. Q. Yu, *Mater. Res. Express.*, 2018, **5**, 065027.

(15) G. D. Zhou, F. Wang, H. L. Wang, S. Kambam, X. Q. Chen and J. Y. Yoon, *ACS Appl. Mater. Inter.*, 2013, **5**, 3275-3280.

(16) R. L. Zhang, S. S. Liang, M. Jin, T. He and Z. Q. Zhang, *Sensor. Actuat. B: Chem.*, 2017, **253**, 196-202.

(17) T. W. Kang, S. J. Jeon, H. I. Kim, J. H. Park, D. Yim, H. R. Lee, J. M. Ju, M. J. Kim and J. H. Kim, *ACS nano*, 2016, **10**, 5346-5353.